Mecánica Computacional Vol XXVI, pp.2800-2819
Sergio A. Elaskar, Elvio A. Pilotta, Germán A. Torres (Eds.)
Córdoba, Argentina, Octubre 2007

COMPUTATIONAL MULTI-FIELD MECHANICS MODEL OF PIEZOELECTRIC MICRORESONATOR ARRAYS

Sergio Preidikman[a,b], He Li[c] and Balakumar Balachandran[c]

[a]Departamento de Estructuras, Facultad de C. E. F. y N., Universidad Nacional de Córdoba, Casilla de Correo 916, 5000 Córdoba, Argentina, spreidik@umd.edu, http://www.efn.uncor.edu
[b]Facultad de Ingeniería, Universidad Nacional de Río Cuarto, Ruta Nacional 36 Km. 601, 5800 Río Cuarto, Argentina, spreidik@umd.edu, http://www.ing.unrc.edu
[c]Department of Mechanical Engineering, University of Maryland at College Park, College Park, MD 20742, USA, balab@umd.edu, http://www.enme.umd.edu/

Keywords: Micromechanical systems, piezoelectric materials, computational multi-field mechanics.

Abstract. *Micromechanical systems (MEMS) that employ active piezoelectric materials, typically in thin-film form, show promise for a variety of applications and are currently the subject of research in a number of laboratories. The development of increasingly complex devices demands sophisticated simulation techniques for design and optimization. MEMS devices typically involve multiple coupled energy domains and media that can be modeled by using a set of partial differential equations, including spatial and time variables. In this work, a computational multi-field mechanics model of a micro-structure with piezoelectric actuation and piezoelectric sensing has been developed as a design tool for micro-resonators and micro-resonator arrays. Although linear models of electrostatically actuated microresonator arrays have been developed in the literature, such models have not been developed for piezoelectrically driven resonator arrays. The developed dynamic model of MEMS resonator array accounts for structural properties and electromechanical coupling effect through finite element analysis. In the simulations, a beam element was used for the structural modeling. We assume that the deflection is large and account for the geometric nonlinearity. The mechanical strain, however, is assumed to be small so that the linear constitutive relations are still valid. The admittance model is derived by combining the linear piezoelectric constitutive equations with the modal transfer function of the resonator structure. The overall transfer function describing the admittance between a driven input and a sense output of a micro-resonator array is obtained in the frequency domain. The resonator receptance matrix is constructed through modal summation by considering only a limited number of dominant modes. The electromechanical coupling determination at the input and output ports makes use of the converse and direct piezoelectric effects. The coupled model can be used to carry out sensitivity studies with respect to the following: (i) the resonator beam thickness and length; (ii) the influence of constant axial forces on the transverse vibrations of clamped-clamped micro-resonator arrays; (iii) geometry of the drive and sense electrodes; and (iv) imperfect boundary conditions due to mask imperfections and fabrication procedure. For micromechanical resonators, these modeling uncertainties come in large part from manufacturing tolerance, residual stresses, irregular surface topology, and material property variations, among others. The developed model has been validated by comparing with results available in the literature for single clamped-clamped resonators.*

1 INTRODUCTION

Microfabrication of filters, switches, choppers, oscillators, and related communication system components has been recognized as a key enabler for increasing functionality while reducing system size and power requirements for mobile communications (Lin et al., 1998; Nguyen, 1999). Compared to traditional surface acoustic wave (SAW) filters and bulk acoustic mechanical resonators, micromechanical resonators are attractive candidates for mobile communications and signal processing applications (e.g., Fourier transform computations), since they offer many benefits including reduction in system size and reduction in power requirements. Microscale polysilicon capacitive filters, which are based on electrostatic actuation and capacitive sensing, have been used to demonstrate devices approaching 100 MHz center frequency with Q factors in the range of 7,500. However, in order to realize filters with center frequencies in the GHz range, the actuation and scaling will need to be scaled to the micron and sub-micron length scales. As the polysilicon resonator dimensions are reduced to the micron and sub-micron length scales, neither the electrostatic actuation characteristics nor the capacitive sensing characteristics scale well. In this regard, piezoelectric actuation and piezoelectric sensing based resonators are attractive for scaling down to micron and sub-micron ranges and realizing filters with high center frequencies. Apart from filters and other signal-processing applications, piezoelectrically driven systems are also viable candidates for micropumps, microjets, and energy reclamation devices.

Microscale polysilicon capacitive filters, which are based on electrostatic actuation and capacitive sensing, have been explored by a number of groups, most notably by C. Nguyen and co-workers [see, for e.g., Nguyen, 1999]. By using this technology, devices approaching 100 MHz with Q factors of 7,500 have been demonstrated (Wang et al., 2000). However, neither electrostatic actuation nor capacitive sensing scale well as resonator dimensions are reduced to the micron and sub-micron length scales as required for filters with center frequencies in the GHz range and other high-frequency resonators.

As demonstrated by DeVoe (2001), piezoelectric actuation and sensing can avoid this problem, and one can take advantage of this to design filters with significantly higher center frequencies. The clamped-clamped beam piezoelectric resonator, which is depicted in Figure 1, is a simple example of such a device. This device uses a thin film piezoelectric layer on the top of a beam structure with input (drive) and output (sense) electrodes positioned on opposite sides of the beam. The composite beam structure is driven at one of its resonances, which is typically the fundamental resonance frequency. The input (drive) voltage generates an electric field between the top and bottom electrodes and induces a strain in the drive side of the resonator through the converse piezoelectric effect. This strain results in a concentrated moment applied at the terminal edge of the input electrode. A bending moment results from the offset of the piezoelectric layer from the beam neutral axis. When the input voltage frequency is near the fundamental frequency of the beam, the beam is in resonance amplifying the piezoelectric strain on the sensing side of the resonator. This induces a current in the sensor circuit at the resonance frequency of the beam through the direct piezoelectric effect. Collaborators at the Army Research Laboratory (ARL), Adelphi, MD and the University of Maryland have demonstrated similar devices based on piezoelectric thin films that operate at 9.2 MHz with Q factors on the order of 1000 (Piekarski et al., 2001).

Above a critical frequency that is dependent on device geometry, the coupling strength of piezoelectric filters becomes significantly larger than capacitive devices. In addition, because current micromechanical and nanomechanical resonators and filters typically rely on electrostatic or magnetic excitation, they suffer from significant limitations on achievable linear dynamic range and impedance. In addition, the piezoelectric resonators can operate at very low power and voltage levels compared to electrostatic devices, which require high-voltage biasing for acceptable electromechanical coupling. If the system behavior is linear, then as described by Ballato (2001) for devices that operate in different energy domains such as electrical and mechanical domains, one can construct an equivalent-circuit representation. This resulting equivalent linear system representation can then be used for the subsequent design. However, when nonlinear effects are pronounced, studies need to be conducted to identify the operational parameter ranges in which this type of linear representations can be used. In order to design and fabricate piezoelectric microelectromechanical resonator systems, a fundamental understanding of the oscillatory characteristics of these systems is needed.

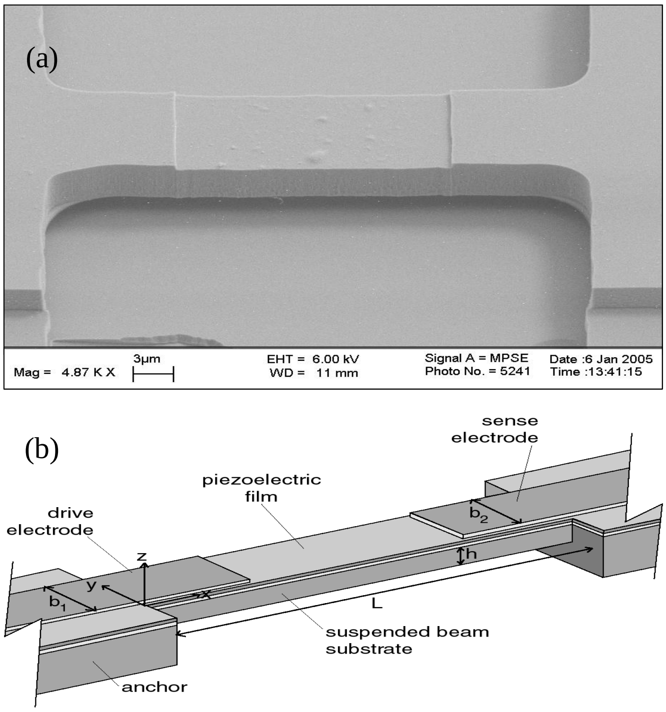

Figure 1: (a) SEM of a PZT resonator (courtesy, Maryland MEMs Laboratory) and (b) a schematic showing the details [DeVoe (2001)].

Two types of resonators are considered here. One type of resonators will be referred to as the AlGaAs resonator, and the other type of resonators will be referred to as the PZT resonator. Both types of resonators are composite structures, and the PZT resonators have asymmetric cross-sections, as discussed in previous work (DeVoe, 2001; Currano, 2002). The considered resonators are based on the piezoelectric effect, as shown in Figure 1. The elastic substrate is a SiO2 layer, on the top of which a platinum electrode layer is deposited throughout the length of the structure. A thin layer of sol-gel piezoelectric film is located on the top of this electrode layer. To complete the structure, another platinum layer is deposited on the top of this piezoelectric film and this layer extends over one quarter of the length from each anchor. The mid-section of the resonator structure is free from this platinum electrode. Due to the asymmetry of the cross section, the position of the piezoelectric layer is offset from the neutral axis, and in addition, (tensional) residual stress may also be introduced in each layer during the fabrication process. The effect of these stresses is explored in this work.

In order to design and fabricate piezoelectric microelectromechanical resonator systems, a fundamental understanding of the oscillatory characteristics of these systems is needed. This work is aimed at developing this fundamental understanding, and in particular, in elucidating the role of nonlinear mechanics in the design of such resonators and arrays of such resonators.

As pointed out in the authors' recent work, the resonators also exhibit non-linear characteristics (Preidikman, 2003; Balachandran and Preidikman, 2004; Balachandran, 2005). These characteristics include Düffing oscillator like response during resonance excitations, temporal harmonics in the response, and spatial patterns during forced oscillations that cannot be explained by conventional linear analysis. The lengths of the resonators considered in previous studies typically range from 100 µm to 400 µm, and the thickness of each platinum electrode is in the range of 90 nm to 180 nm. In some typical uses of this resonator, the structure is driven close to its first resonance frequency with the input at the drive electrode having a DC bias in addition to the harmonic component. In this work, the authors discuss a semi-analytical finite element based formulation, in which transverse free vibrations of composite, and axially stepwise varying properties micro-resonators and micro-resonator arrays subjected to constant axial loads are considered (see Figure 2 for a clamped-clamped case). It is shown that the consideration of axial loads is important to predict the natural frequencies of the resonators observed in the experiments.

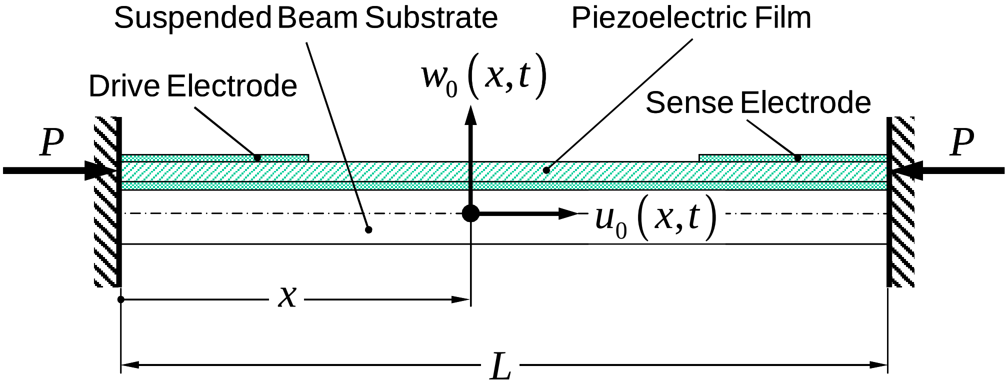

Figure 2: Clamped-clamped composite resonator subjected to a constant axial load P.

In the last several years, there has been a growing need for accurate modeling and simulation of microelectromechanical devices and systems that employ piezoelectric materials. This comes from the need to reduce design iterations and speed up the product development, and also to ensure reliability of the final product. Finite element analysis (FEA) plays an important role in the simulation of MEMs devices, and this analysis generally covers multiple domains for a single device, such as structural, thermal, electrostatic, electromagnetic, and fluid domains. von Preissig and Kim (2000) examined techniques for modeling thin-piezoelectric MEMs devices by using existing finite-element packages. In this work, piezoelectrically actuated bending is examined. The authors point out that, while it may seem that the sheet-like nature of structures in piezoelectric MEMs would make them good candidates for conducting FEA with plate elements, solid or "brick" elements can work remarkably well. Finite element model (FEM) errors associated with the discretization of the model have also been analyzed. An important issue to note is that meshing a thin sheet into low-aspect-ratio elements requires a prohibitively large number of elements, while too low a mesh density might result in severe discretization and element-shape errors. A four-node, isoparametric, linear piezoelectric, plane-strain element from the ANSYS library has been used in this work. Wang and Ostergaard (1999) used finite elements to develop a coupled simulation method for piezoelectric transducers with an attached electric circuit. In this work, the weak form of the laws of conservation of momentum and electric charge for a linear piezoelectric medium are discretized by using FEM. Their method has been implemented in the ANSYS software. Chen et al. (2002) presented a two-dimensional analytical model of a spiral-shaped PZT ceramic actuator. They used FEA to validate the results obtained from analytical model. In this work, the commercially available software packages PATRAN and ABAQUS are used. PATRAN is utilized as the pre-processor and ABAQUS is used as a post-processor to perform the linear elastic, piezoelectric analysis. In order to capture bending effects accurately, the authors used eight-noded, isoparametric, plane strain, linear elastic, piezoelectric elements. For achieving convergence, while keeping the length-to-width ratio of the elements reasonable, they used meshes with at least 10 elements across the spiral thickness. A typical finite element mesh of a two-turn spiral actuator has more than 3000 elements.

In this work, the coupling of electrical and mechanical fields that is intrinsic to a piezoelectric material is accomplished in a non-traditional approach. From a filter design standpoint, the admittance function relating input voltage to output current $I_m(\omega)/V_n(\omega)$ is an important frequency-response function to be determined (see Figure 3).

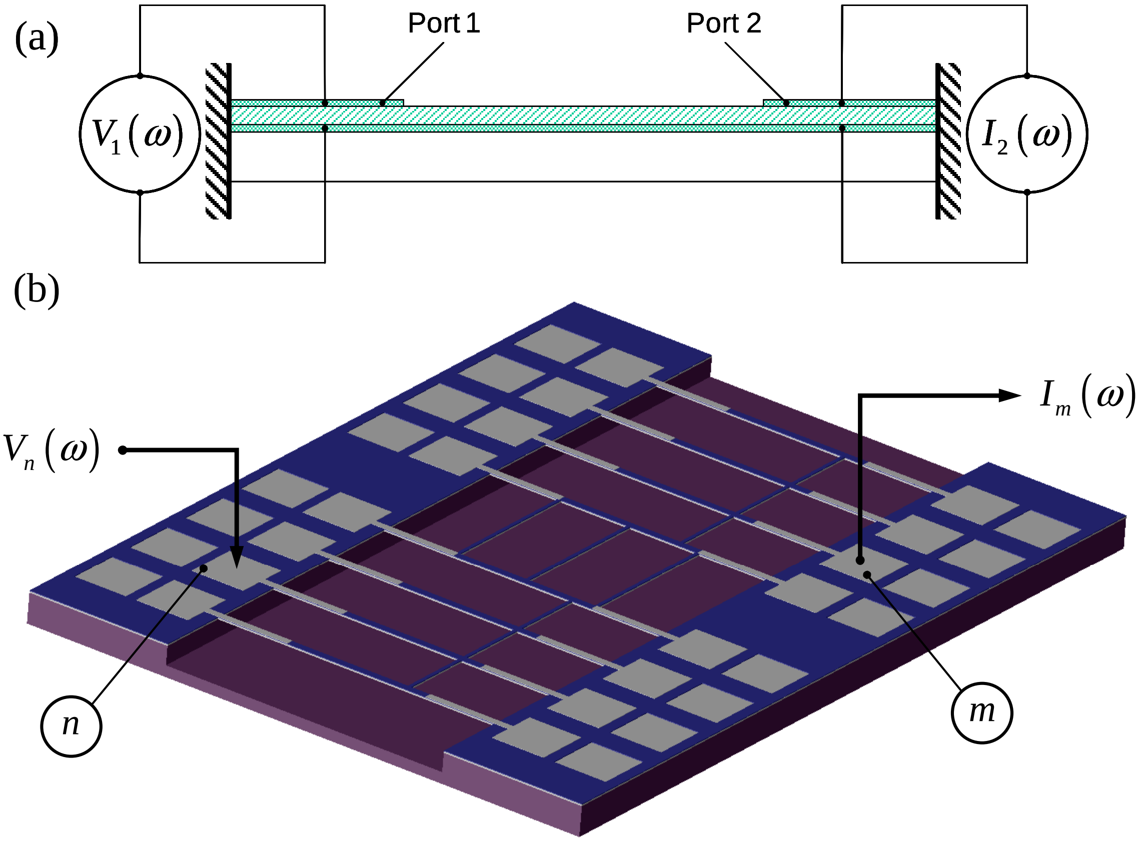

Figure 3: Input and output quantities of interest for: (a) a clamped-clamped piezoelectric microresonator, and (b) a clamped-clamped piezoelectric microresonator array.

This admittance function may be obtained by relating the mechanical transfer function of the microresonator structure to the corresponding electrical input and output through the piezoelectric constitutive equations. In the second section of this work, this admittance function is determined for a composite microresonator with axially stepwise varying properties. This microresonator is also subjected to constant axial loads. The obtained admittance function has the form

$$Y_{mn}(\omega)=\frac{I_m(\omega)}{V_n(\omega)}=\mathbf{C}^S(\omega)\mathbf{H}^{SA}(\omega)\mathbf{F}^A \tag{1}$$

where $\mathbf{H}^{SA}(\omega)$ is a “block” of the complex frequency response matrix for the considered microresonator (e.g., Preidikman and Balachandran, 2006); $\mathbf{C}^S(\omega)$ is a matrix that depends on the material properties of the PZT material, the geometry of the sensor, and the finite element discretization of the microresonator; and $\mathbf{F}^A$ is a vector that depends on the material properties of the PZT, the geometry of the actuator, the geometry of the suspended beam substrate, and the finite element discretization of the microresonator. Comparisons with experimental results and results available in the literature are presented. It is believed that the numerical and analytical efforts presented in this work can be used as a basis to develop design tools for piezoelectric microresonators and microresonator arrays.

2 SEMI-ANALYTICAL TOOL BASED ON GEOMETRIC NONLINEARITIES FOR MICRORESONATOR ARRAYS DESIGN

In this effort, a computational multi-field mechanics model of a micro-structure with piezoelectric actuation and piezoelectric sensing has been developed as a design tool for micro-resonators and micro-resonator arrays. The developed model accounts for the structural properties and the electromechanical coupling effect through finite element analysis. It is assumed that the deflection is large and that the geometric nonlinearity must be included. The dynamic admittance model is derived by combining the linear piezoelectric constitutive equations with the modal transfer function of the multi-layered microresonator structure. The resonator receptance matrix is constructed through modal summation by considering a limited number of dominant modes. The electromechanical coupling determination at the input and output ports makes use of the converse and direct piezoelectric effects. In the development of the finite-element models, the boundary conditions, the shapes of electrodes, and distributed parameters such as varying elastic modulus across the length of the structure have been taken into account. The developed semi-analytical tool can be used to carry out parametric studies with respect to the following: (i) the resonator beam thickness and length; (ii) the influence of constant axial forces on the transverse vibrations of clamped-clamped microresonators; (iii) the geometry of the drive and sense electrodes; and (iv) imperfect boundary conditions due to mask imperfections and fabrication procedure. The semi-analytical development has been validated by comparing the model predictions with prior results available in the literature for clamped-clamped resonators and experimental measurements.

2.1 The equations of motion in the frequency domain

The equations of motion of the microresonator array in the frequency domain are of the form

$$\left\{-\omega^2\mathbf{M}+j\,\omega\mathbf{C}+\mathbf{K}\right\}\mathbf{d}(\omega)=\mathbf{f}(\omega) \tag{2}$$

where $j=\sqrt{-1}$, $\mathbf{K}=\mathbf{K}_E+\mathbf{K}_G$ is the global stiffness matrix, $\mathbf{M}$, $\mathbf{K}_E$ and $\mathbf{K}_G$ are the global mass matrix, elastic stiffness matrix, and geometrical stiffness matrix, respectively, and $\mathbf{d}(\omega)$ and $\mathbf{f}(\omega)$ are the Fourier transforms of the nodal displacements $\mathbf{d}(t)$ and the nodal forces $\mathbf{f}(t)$, respectively. The development of the time-domain model with the geometric nonlinearity is detailed in Preidikman and Balachandran, 2006. From (2), one obtains

$$\mathbf{d}(\omega)=\mathbf{H}(\omega)\mathbf{f}(\omega) \tag{3}$$

where

$$\mathbf{H}(\omega)=\left\{-\omega^2\mathbf{M}+j\,\omega\mathbf{C}+\mathbf{K}\right\}^{-1} \tag{4}$$

is the complex frequency response matrix (the mechanical force-displacement transfer function) of the beam micro-resonator (Preidikman and Balachandran, 2006). Since proportional damping is assumed, the complex frequency response matrix can be constructed from the modal summation as

$$\mathbf{H}(\omega)=\left[H_{rs}(\omega)\right]=\left[\sum_{l=1}^{n_{\text{mod}}}\frac{\phi_{lr}\phi_{ls}}{\omega_l^2\left[1-\left(\omega/\omega_l\right)^2+j2\zeta_l\left(\omega/\omega_l\right)\right]}\right] \tag{5}$$

where $r,s=1,2,\ldots,n_{dof}$, n_{dof} is the number of degrees of freedom (dof) of the finite element model, ω_l is the lth natural frequency of the undamped system, and ζ_l is the lth damping ratio of the microresonator. In (5), ϕ_{lr} and ϕ_{ls} are, respectively, the *r*-component and the *s*-component of the *l*th mass normalized mode shape of the microresonator. Further, in (5), n_{mod} is the number of dominant modes.

The damping ratio in (5) is, in general, determined experimentally from the measured quality factor, Q_l, which is given by,

$$Q_l=\frac{\sqrt{\Omega_{cu}\Omega_{cl}}}{\Omega_{cu}-\Omega_{cl}} \tag{6}$$

where the cutoff frequencies are given by

$$\Omega_{cl}=\sqrt{1-2\zeta_l^2-2\zeta_l\sqrt{1-\zeta_l^2}}\quad\text{and}\quad\Omega_{cu}=\sqrt{1-2\zeta_l^2+2\zeta_l\sqrt{1-\zeta_l^2}} \tag{7}$$

After substituting from (7) into (6) and using a Taylor's series expansion about $Q_l=0$, the result obtained is

$$Q_l=\frac{1}{2\zeta_l}-\frac{3}{2}\zeta_l-\frac{9}{4}\zeta_l^3+O(\zeta_l^4) \tag{8}$$

Hence, for very lightly damped microresonators (high-*Q* microresonators); that is $0<\zeta<<1$, the quality factor can be approximated as

$$Q_l\cong\frac{1}{2\zeta_l} \tag{9}$$

Now, in terms of the quality factors it is possible to rewrite the degree of freedom (dof)-to-dof mechanical complex frequency response function of the microresonator structure,

$H_{rs}(\omega)$, as

$$H_{rs}(\omega) = \sum_{l=1}^{n_{\text{mod}}} \frac{\phi_{lr}\phi_{ls}}{\omega_l^2\left[1-\left(\frac{\omega}{\omega_l}\right)^2 + j\frac{1}{Q_l}\left(\frac{\omega}{\omega_l}\right)\right]} \tag{10}$$

At this point, one has the elements of the complex frequency response matrix, which describes the resulting harmonic displacement of the *r*th dof caused by a unit harmonic force applied at the *s*th dof.

2.2 Admittance Model

In this section, a semi-analytical model describing the admittance function for a clamped-clamped piezoelectric microresonator is developed. The semi-analytical admittance model may be obtained by relating the (numerical) mechanical transfer function of the microresonator structure to the corresponding electrical input and output through the (analytical) piezoelectric constitutive equations. The overall frequency-response function describing the admittance $Y_{21}(\omega)$ between the driven input (port 1) and the sense output (port 2) of the beam resonator shown Figure 1 is defined as

$$Y_{21}(\omega) = \frac{I_2(\omega)}{V_1(\omega)} \tag{11}$$

where $V_1(\omega)$ is the voltage applied to the input port, and $I_2(\omega)$ is the current measured at the output port.

2.3 Actuator Side

In this work, the active film under consideration is considered to be long, narrow, and thin, so as to make the length L_1 much greater than the maximum value of the width $b_1(x)$, which is much greater than the thickness h_p (Figure 4).

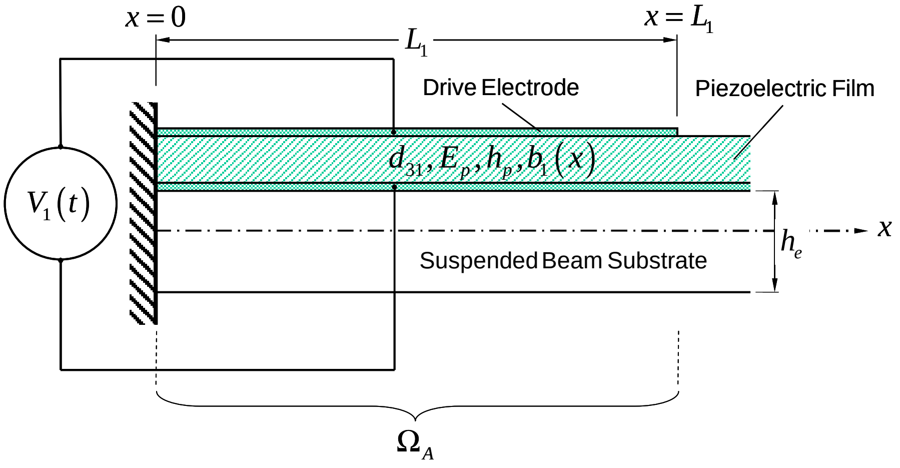

Figure 4: Schematic view of the actuator port.

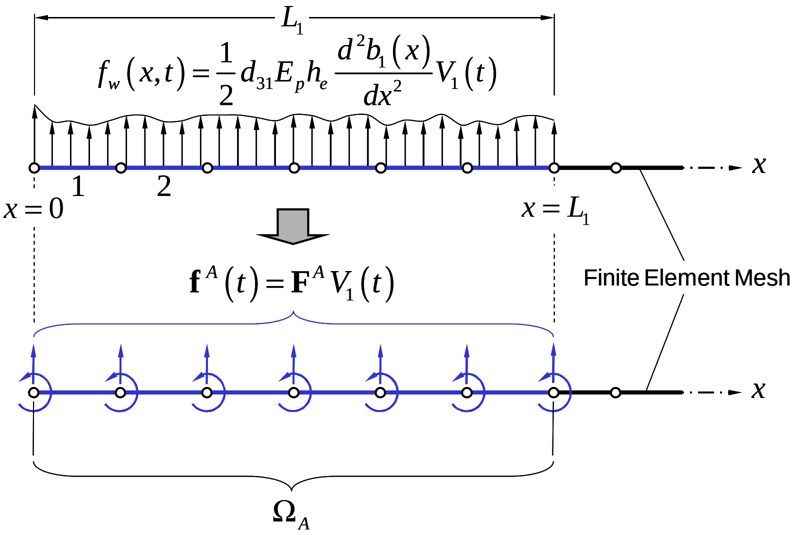

Figure 5: External, transverse distributed force and generalized finite element nodal forces.

Next, attention is focused on the case when the active film is driven by an AC voltage $V_1(t)$. The externally transverse distributed force $f_w(x,t)$ can be expressed in terms of the drive voltage $V_1(t)$ as

$$f_w(x,t)=\frac{1}{2}d_{31}E_ph_e\frac{d^2b_1(x)}{dx^2}V_1(t)H(x) \tag{12}$$

where $H(x)=U(x)-U(x-L_1)$, and $U(x-a)$ is the Heaviside step function. The basis for (12) is detailed in Preidikman and Balachandran, 2006. In view of (12), the generalized element nodal forces, $\mathbf{f}_1^e(t)$ and $\mathbf{f}_2^e(t)$ can be written in terms of the drive voltage $V_1(t)$ as

$$\begin{aligned}&\mathbf{f}_1^e(t)=\mathbf{0}_{2\times1},\\&\mathbf{f}_2^e(t)=\left\{\frac{1}{2}d_{31}E_ph_e\int_{\Omega_e}\frac{d^2b_1(x)}{dx^2}\mathbf{N}_2(x)dx\right\}V_1(t),\quad \Omega_e\subseteq\Omega_A\end{aligned} \tag{13}$$

where $\mathbf{N}_2(x)$ is a shape function matrix, as discussed in Preidikman and Balachandran, 2006. Further, $\Omega_A=\{x\,|\,0\le x\le L_1\}$ denotes the sub-domain of $[0,L]$ occupied by the sensor (**¡Error! No se encuentra el origen de la referencia.**). In the frequency domain, (13) becomes

$$\mathbf{f}_1^e(\omega)=\mathbf{0}_{2\times1},\quad \mathbf{f}_2^e(\omega)=\mathbf{F}_2^eV_1(\omega),\quad \Omega_e\subseteq\Omega_A \tag{14}$$

where, $V_1(\omega)$, $\mathbf{f}_1^e(\omega)$, and $\mathbf{f}_2^e(\omega)$ are the Fourier transforms of $V_1(t)$, $\mathbf{f}_1^e(t)$, and $\mathbf{f}_2^e(t)$, respectively, and $\mathbf{F}_2^e$ is the frequency-independent vector of generalized element nodal forces defined as

$$\mathbf{F}_2^e=\frac{1}{2}d_{31}E_ph_e\int_{\Omega_e}\frac{d^2b_1(x)}{dx^2}\mathbf{N}_2(x)dx,\qquad \Omega_e\subseteq\Omega_A \tag{15}$$

By using (14) and the assembly operator, the sub-vector of generalized equivalent nodal forces can be written as follows,

$$\mathbf{f}^{A}(\omega)=\underset{e}{\mathbf{A}}\begin{Bmatrix}\mathbf{0}_{2\times 1}\\ \mathbf{F}_{2}^{e}\end{Bmatrix}V_{1}(\omega)=\mathbf{F}^{A}V_{1}(\omega),\qquad e\in\Omega_{A} \tag{16}$$

2.4 Sensor Side

On the sensor side, the attention is focused on the direct piezoelectric effect. As described before, a key to developing a useful electromechanical model of a piezoelectric model is the determination of changes in electrode charges when the active film is strained due to the mechanical excitation of the microresonator. At the sensor port, it is also considered that the active film is long, narrow, and thin, so as to make the length L_2 much greater than the maximum value of the width $b_2(x)$, which in turn is much greater than the thickness h_p (Figure 6).

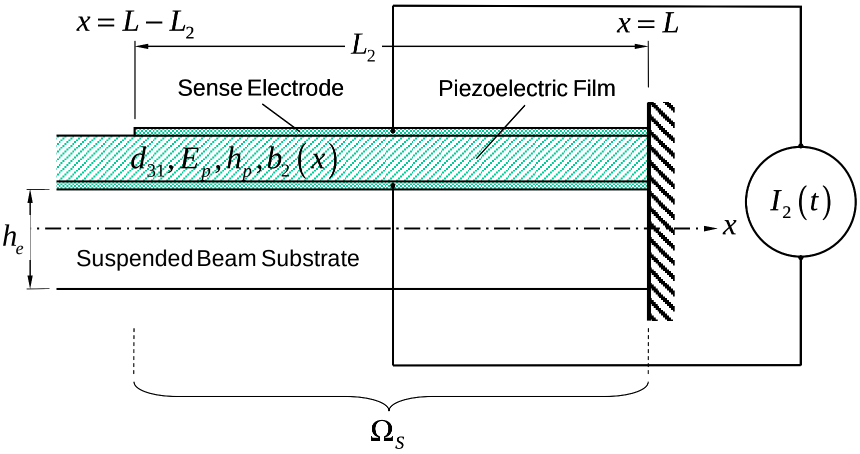

Figure 6: Schematic view of the sensor port.

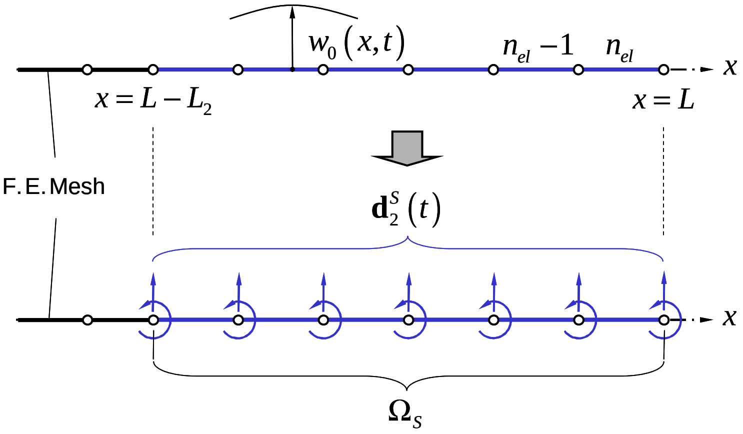

Figure 7: Transverse displacements of the centroidal axis and generalized finite element nodal displacements.

Considering the relation between the output charge and the output current, in the frequency domain, the expression for the output current becomes

$$I_2\left(\omega\right) = j\omega Q_2\left(\omega\right) = j\omega d_{31} E_p \int_{L-L_2}^{L} b_2\left(x\right)\left[\frac{\partial u_0\left(x,\omega\right)}{\partial x} - \frac{h_e}{2}\frac{\partial^2 w_0\left(x,\omega\right)}{\partial x^2}\right]dx \tag{17}$$

The integral in (17) can be split as

$$\begin{aligned}
&\int_{L-L_2}^{L} b_2\left(x\right)\frac{\partial u_0\left(x,\omega\right)}{\partial x}dx = \sum_e \int_{\Omega_e} b_2\left(x\right)\frac{\partial u_0\left(x,\omega\right)}{\partial x}dx,\\
&\int_{L-L_2}^{L} b_2\left(x\right)\frac{\partial^2 w_0\left(x,\omega\right)}{\partial x^2}dx = \sum_e \int_{\Omega_e} b_2\left(x\right)\frac{\partial^2 w_0\left(x,\omega\right)}{\partial x^2}dx,\\
&\Omega_e \subseteq \Omega_S
\end{aligned} \tag{18}$$

where $\Omega_S = \left\{x \mid L - L_2 \le x \le L\right\}$ denotes the sub-domain of $\left[0, L\right]$ occupied by the sensor port (Figure 7). Hence the expression for the output current becomes

$$I_2\left(\omega\right) = \sum_e \left[\mathbf{A}^e\left(\omega\right)\mathbf{d}_1^e\left(\omega\right) + \mathbf{B}^e\left(\omega\right)\mathbf{d}_2^e\left(\omega\right)\right] = \mathbf{C}^S\left(\omega\right)\mathbf{d}^S\left(\omega\right), \quad e \in \Omega_S \tag{19}$$

where the sub-matrices $\mathbf{A}^e\left(\omega\right)$ and $\mathbf{B}^e\left(\omega\right)$ are given by

$$\begin{aligned}
\mathbf{A}^e\left(\omega\right) &= j\,\omega d_{31} E_p \int_{\Omega_e} b_2\left(x\right)\frac{\partial \mathbf{N}_1\left(x\right)}{\partial x}dx, \quad \forall \Omega_e \subseteq \Omega_S\\
\mathbf{B}^e\left(\omega\right) &= -j\,\omega \frac{h_e}{2} d_{31} E_p \int_{\Omega_e} b_2\left(x\right)\frac{\partial^2 \mathbf{N}_2\left(x\right)}{\partial x^2}dx, \quad \forall \Omega_e \subseteq \Omega_S
\end{aligned} \tag{20}$$

At this point, it is convenient to rewrite the system (2) in the following block-partitioned form

$$\left\{\begin{array}{c}
\mathbf{d}^A\left(\omega\right)\\ \hdashline
\mathbf{d}^M\left(\omega\right)\\ \hline
\mathbf{d}^S\left(\omega\right)
\end{array}\right\} = \left[\begin{array}{c|c:c}
\mathbf{H}^{AA}\left(\omega\right) & \mathbf{H}^{AM}\left(\omega\right) & \mathbf{H}^{AS}\left(\omega\right)\\ \hdashline
\mathbf{H}^{MA}\left(\omega\right) & \mathbf{H}^{MM}\left(\omega\right) & \mathbf{H}^{MS}\left(\omega\right)\\ \hline
\mathbf{H}^{SA}\left(\omega\right) & \mathbf{H}^{SM}\left(\omega\right) & \mathbf{H}^{SS}\left(\omega\right)
\end{array}\right]\left\{\begin{array}{c}
\mathbf{f}^A\left(\omega\right)\\ \hline
\mathbf{f}^M\left(\omega\right)\\ \hdashline
\mathbf{f}^S\left(\omega\right)
\end{array}\right\} \tag{21}$$

where A stands for "Actuator", M for "Midspan", and S for "Sensor" (Figure 8).

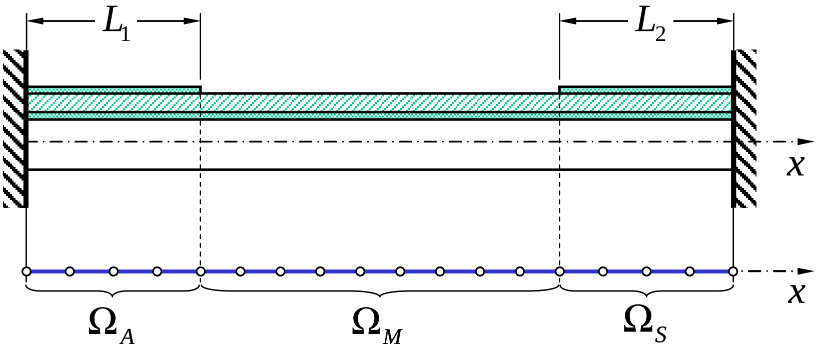

Figure 8: Schematic view of the clamped-clamped piezoelectric microresonator and the finite element mesh.

By considering that in the present case, both $\mathbf{f}^M\left(\omega\right)$ and $\mathbf{f}^S\left(\omega\right)$ are equal to zero, and using (16), it is possible to express $\mathbf{d}^S(\omega)$ in terms of the mechanical force-displacement transfer function and the driven voltage as follows

$$\mathbf{d}^S(\omega) = \mathbf{H}^{SA}(\omega)\mathbf{f}^A(\omega) = \mathbf{H}^{SA}(\omega)\mathbf{F}^A V_1(\omega) \tag{22}$$

Finally, combining (24) and (19), the admittance function relating input voltage to output current, can be expressed as

$$Y_{21}(\omega) = \frac{I_2(\omega)}{V_1(\omega)} = \mathbf{C}^S(\omega)\mathbf{H}^{SA}(\omega)\mathbf{F}^A \tag{23}$$

3 EXPERIMENTAL RESULTS, COMPARISONS, AND DISCUSSION

The developed coupled model enables one to investigate the following: i) the elastic stability of the resonator, ii) the influence of a constant axial force on the transverse vibrations of a clamped-clamped resonator structure, and iii) the influence of a constant axial force on the transverse vibrations of a free-free structure.

3.1 Prestressed Microresonators

A case of interest is one where the geometric stiffness is driven by a parameter λ; for example, in the case of a microresonator subjected to an initial axial force P_0 due to residual stresses introduced during the fabrication of the resonators.

3.2 Influence of a constant axial force on the transverse vibrations of a clamped-clamped resonator structure

In Figure 9, for a clamped-clamped AlGaAs resonator, the variations of the first four natural frequencies are shown with respect to the axial load. As expected, as the axial stretching load increases, the natural frequencies increase. Similarly, they decrease with the increase of the compressive axial load.

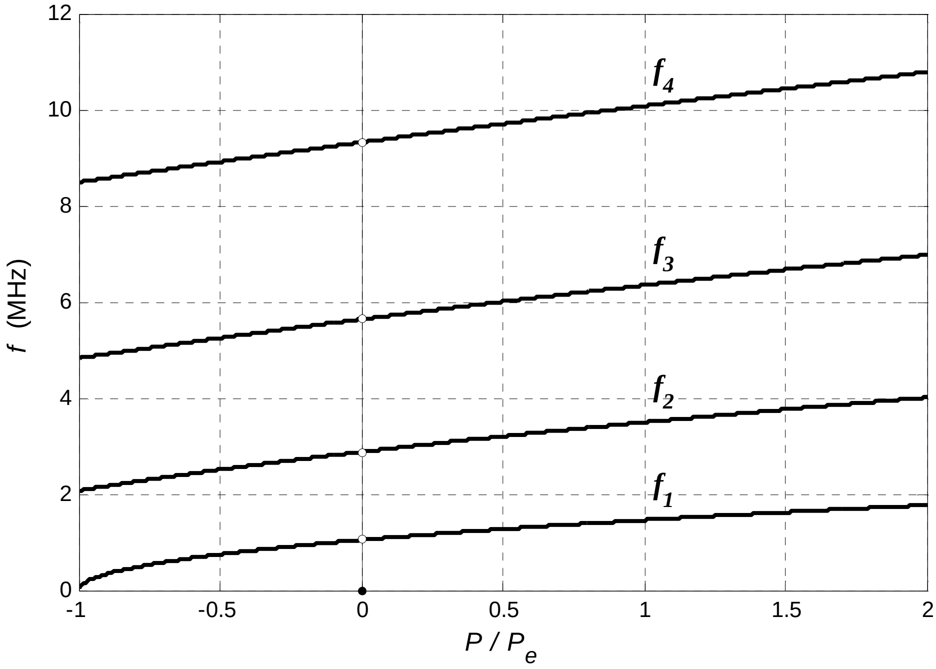

Figure 9: Variations of natural frequencies with axial load for a AlGaAs micro-resonator.

When the compressive axial force reaches the value of the Euler's buckling load, $P_{cr} = 1.2489E\text{-}2\ \text{N}$, the first natural frequency goes to zero. The composite material properties and layer thickness values for the considered AlGaAs resonators are listed in Table 1. Each AlGaAs microresonator has a particular orientation on the wafer. The orientation on the wafer is indicated, with respect to a reference orientation, by the so-called "wafer-angle" and this in turn leads to a certain crystallographic direction of the AlGaAs structure. The variation of the first natural frequency shown in Table 2 has been obtained from experimental measurements for different resonators.

As a representative example, a 100 μm long resonator with a 15 μm width is considered. From the results shown in Figure 10, it can be seen that the numerically calculated value of the first natural frequency is $1501.5\ \text{kHz}$, in the absence of axial stresses. The first natural frequency value shifts to $1319.3\ \text{kHz}$, when the experimentally obtained values of residual stresses are included in the model. In Figure 11, an expanded plot of a portion of Figure 10 is shown. The horizontal lines represent the experimentally obtained values of the first natural frequency corresponding to the 100 μm resonator for different wafer angles. It can be seen that the numerically obtained values fall within the range of experimental measurements, which are listed in Table 2.

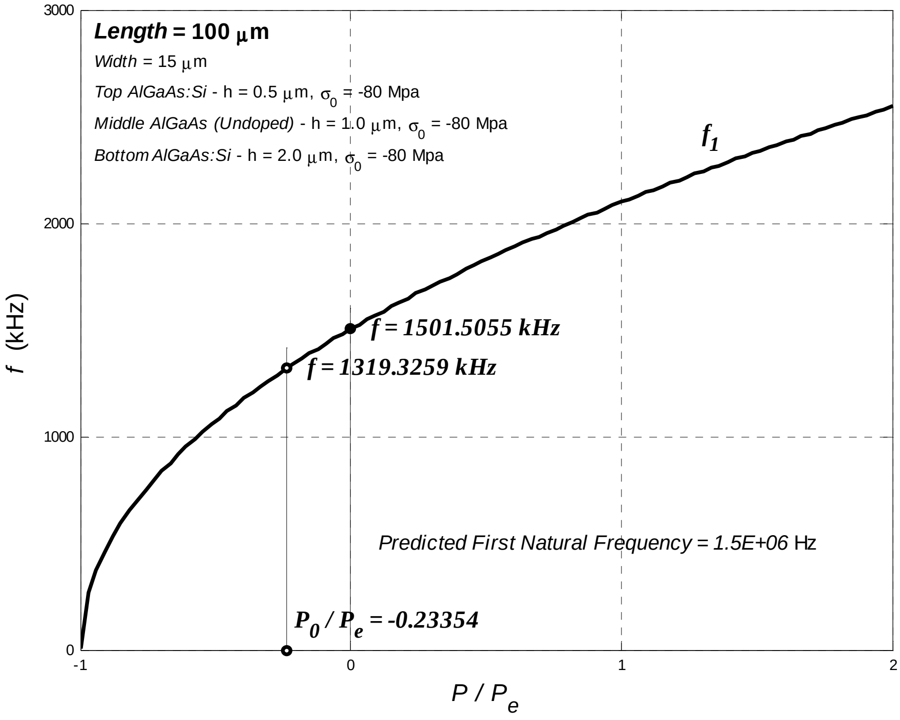

Figure 10: Variation of the first natural frequency with axial load for a clamped-clamped AlGaAs resonator.

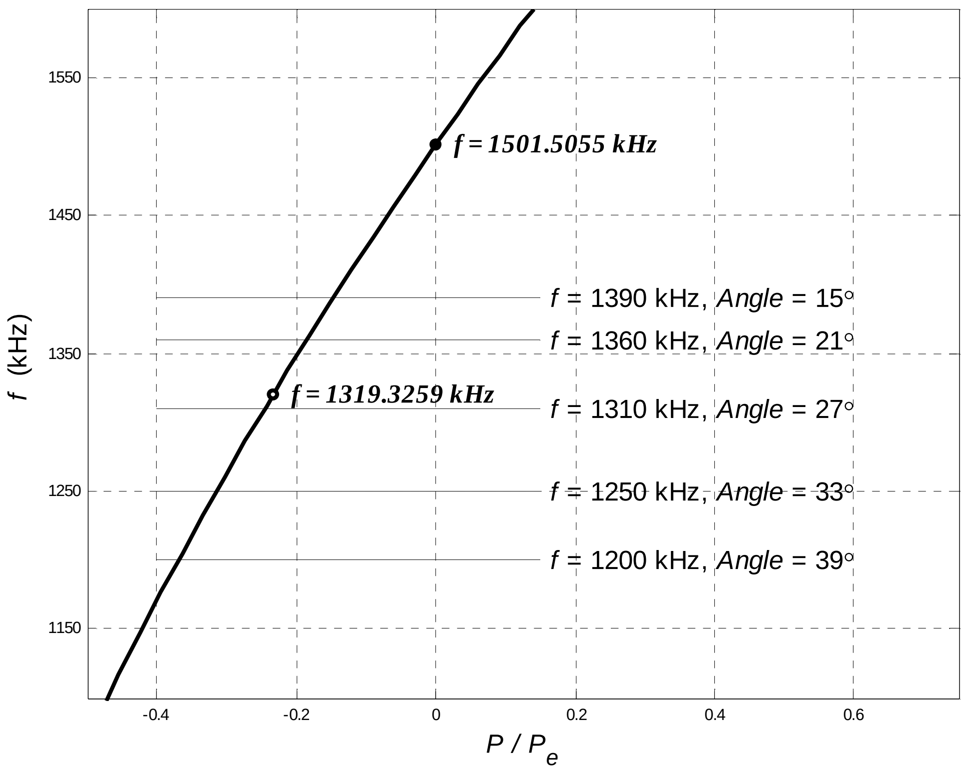

Figure 11: Expanded plot of Figure 10 in the vicinity of the first natural frequency of the AlGaAs resonator predicted without residual stresses.

Layer	Thickness h_k	Residual Stress σ_0 [MPa]
Top AlGaAs:Si	0.5 μm	–80
Middle AlGaAs (Undoped)	1.5 μm	–80
Bottom AlGaAs:Si	2.0 μm	–80

Table 1: Characteristics of AlGaAs resonator.

Angle Length	15°	21°	27°	33°	39°
80 μm	2130 kHz	2070 kHz	2040 kHz	1970 kHz	1890 kHz
100 μm	1390 kHz	1360 kHz	1310 kHz	1250 kHz	1200 kHz
120 μm	960 kHz	920 kHz	900 kHz	860 kHz	830 kHz

Table 2: Experimentally obtained first natural frequencies for different resonator lengths and wafer angles.

3.3 Imperfect boundary conditions due to mask imperfections and fabrication procedure

As a second example, the effect of a 2.5 μm to 5 μm undercut introduced in each resonator anchor by the etching processes during fabrication is considered (for illustrative purposes only, please, see Figure 12).

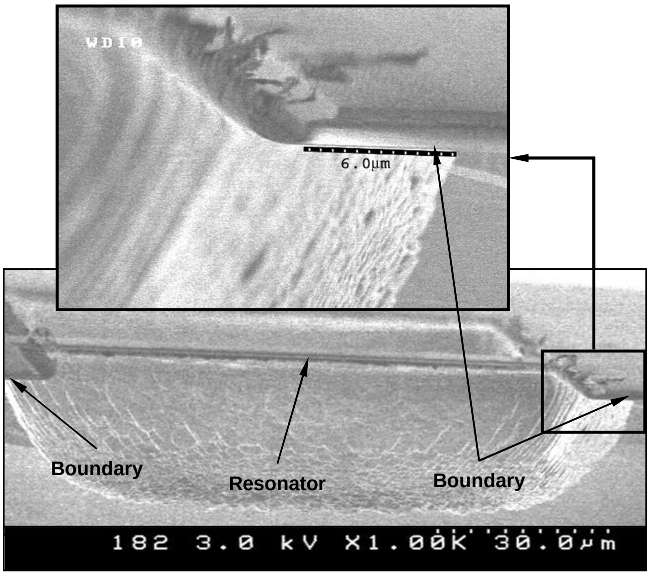

Figure 12: SEM of undercut introduced in a resonator anchor by the etching processes during fabrication [Courtesy, ARL, Adelphi, Maryland].

Resonators of 105 μm and 110 μm lengths were studied to model the effect of the undercut. In Figure 13, the variation of the first natural frequency with respect to the axial load is shown for 100 μm, 105 μm, and 110 μm long microresonators. The experimentally obtained values of the first natural frequencies are also shown in the figure as horizontal lines for making the comparisons. In Figure 14, an expanded portion of Figure 13 is shown around the 1400 kHz range.

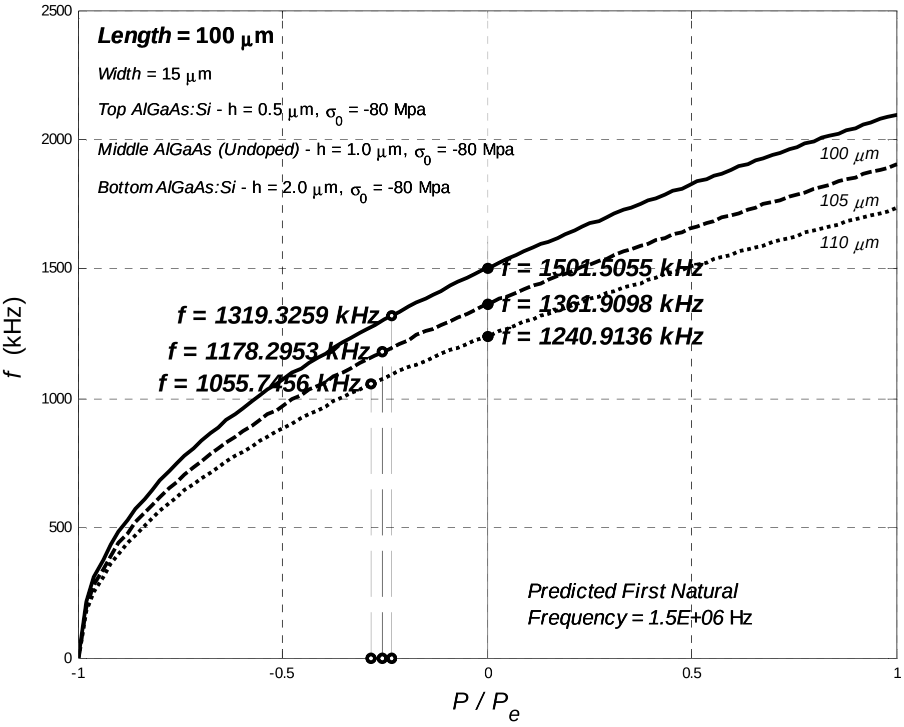

Figure 13: Variation of first natural frequency with axial load P/P_e for a clamped-clamped AlGaAs resonator.

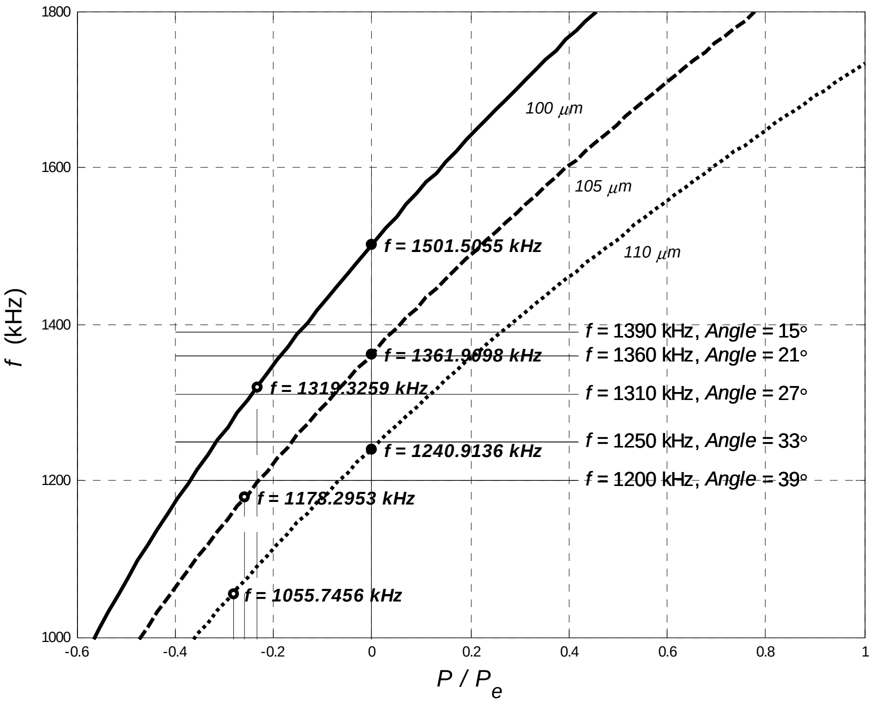

Figure 14: Expanded plot of Figure 13 around 1400 kHz .

Here, the undercut has been simply modeled as an increase in the extension of microresonator length. The change in cross-section area is not considered in this one-dimensional model. This effect has been included in a series of two-dimensional models developed by the authors, and in these models, it is recognized that the undercut region can not be just modeled as a beam. Rather, a more refined finite element model with plate elements needs to be used to model more realistic boundary conditions which include changes in the cross-section area.

3.4 Predictions of frequency response

The shapes of the drive and sense electrodes affect the resonator admittance through $b_1(x)$ and $b_2(x)$. For the resonators shown in this work, maximum electromechanical coupling is desired; that is, the electrodes must be shaped such that $Y_{21}(\omega)$ is maximized. This may be achieved by clipping the electrodes at the quarter beam points, as depicted in Figure 1b. For this electrode geometry, $b_1(x)$ and $b_2(x)$ can be written as

$$b_1(x) = b\left[U(x) - U\left(x - \frac{L}{4}\right)\right] = b\,g_1(x) \text{ and } b_2(x) = b\left[U\left(x - \frac{3L}{4}\right) - U(x-L)\right] = b\,g_2(x) \quad (24)$$

where b is the nominal width of both electrodes and $U(x)$ is the Heaviside unit step function. By using (24), the terms involving the electrodes shapes simplify to

$$\mathbf{F}_2^e = \left(\frac{1}{2} d_{31} E_p h_e b\right) \int_{\Omega_e} \frac{d^2 g_1(x)}{dx^2} \mathbf{N}_2(x)\, dx \quad (25)$$

and

$$\begin{aligned}\mathbf{A}^e(\omega) &= j\,\omega\left(\frac{1}{2}h_e d_{31} E_p b\right)\frac{2}{h_e}\int_{\Omega_e} g_2(x)\frac{\partial \mathbf{N}_1(x)}{\partial x}dx \\ \mathbf{B}^e(\omega) &= -j\,\omega\left(\frac{1}{2}h_e d_{31} E_p b\right)\int_{\Omega_e} g_2(x)\frac{\partial^2 \mathbf{N}_2(x)}{\partial x^2}dx\end{aligned} \qquad (26)$$

In Figure 17 for a $400\,\mu\text{m}$ doubly-clamped AlGaAs resonator with quarter-beam electrodes, the response (magnitude and phase of the normalized admittance function $Y_{21}(\omega)\Big/\left(\frac{1}{2}d_{31}E_p h_e b\right)^2$) are shown for three different values of the axial load. As expected, as the axial stretching load increases, the first natural frequency increases. Similarly, it decreases with the increase of the compressive axial load. The composite material properties and layer thickness values for the considered AlGaAs resonators are listed in Table 1.

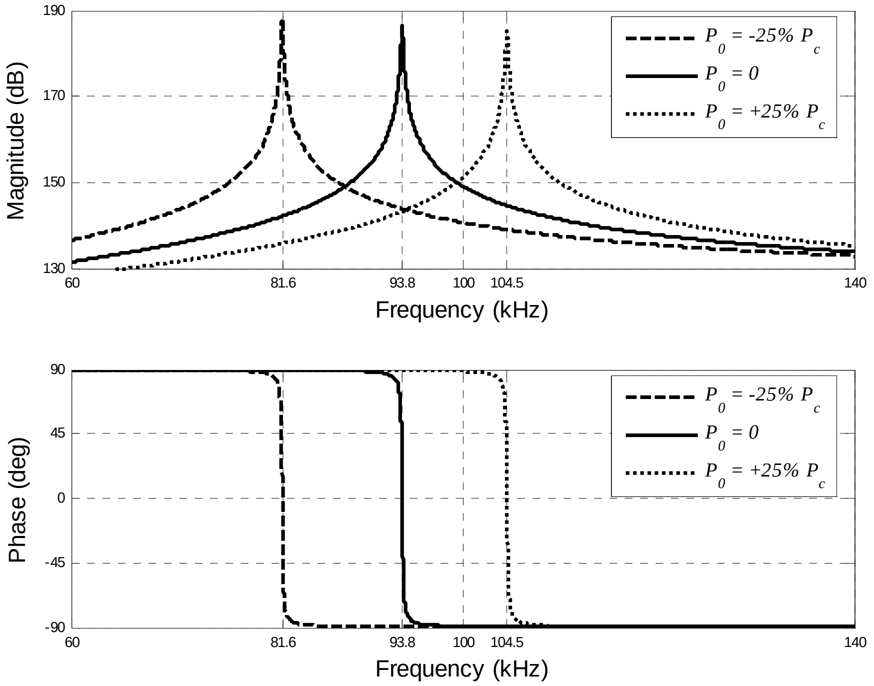

Figure 15: Response of a $400\,\mu\text{m}$ AlGaAs resonator for three different values of the axial load.

3.5 Analyses of Microresonator Arrays

Linear analyses have been carried out to determine the responses of micro-resonator arrays to different excitation conditions. The admittance functions of clamped-clamped AlGaAs resonator arrays (e.g., Figure 16) are being studied to aid the analysis and design of these devices. In Figure 17 representative amplitude response of two doubly-clamped AlGaAs composite beam resonator arrays is shown. Axial loads, to tune or detune composite micro-resonator arrays, were used. The natural frequencies were shifted by applying a DC offset in the input to the drive electrodes. In Figure 18 representative admittance functions of a 40 doubly-clamped AlGaAs composite beam resonator array are shown.

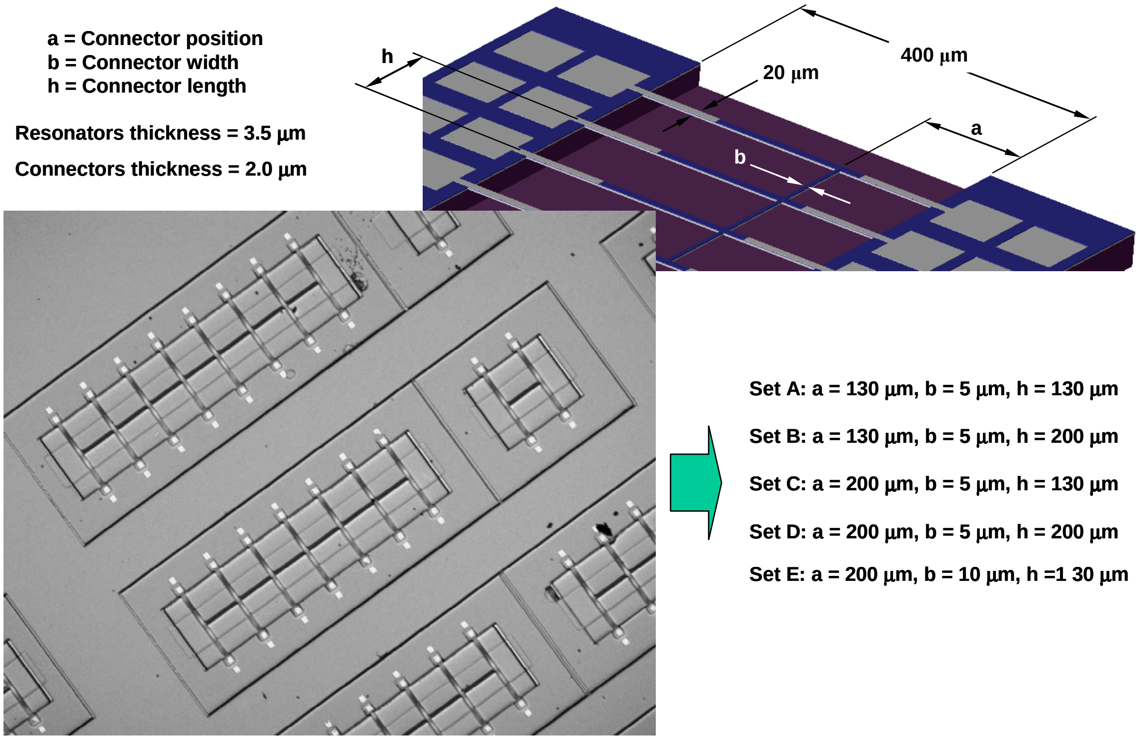

a = Connector position
b = Connector width
h = Connector length

Resonators thickness = 3.5 µm

Connectors thickness = 2.0 µm

Set A: a = 130 µm, b = 5 µm, h = 130 µm

Set B: a = 130 µm, b = 5 µm, h = 200 µm

Set C: a = 200 µm, b = 5 µm, h = 130 µm

Set D: a = 200 µm, b = 5 µm, h = 200 µm

Set E: a = 200 µm, b = 10 µm, h =1 30 µm

P. Kumar, Maryland MEMS Laboratory

Figure 16: A sketch map of the composite micro-resonator array.

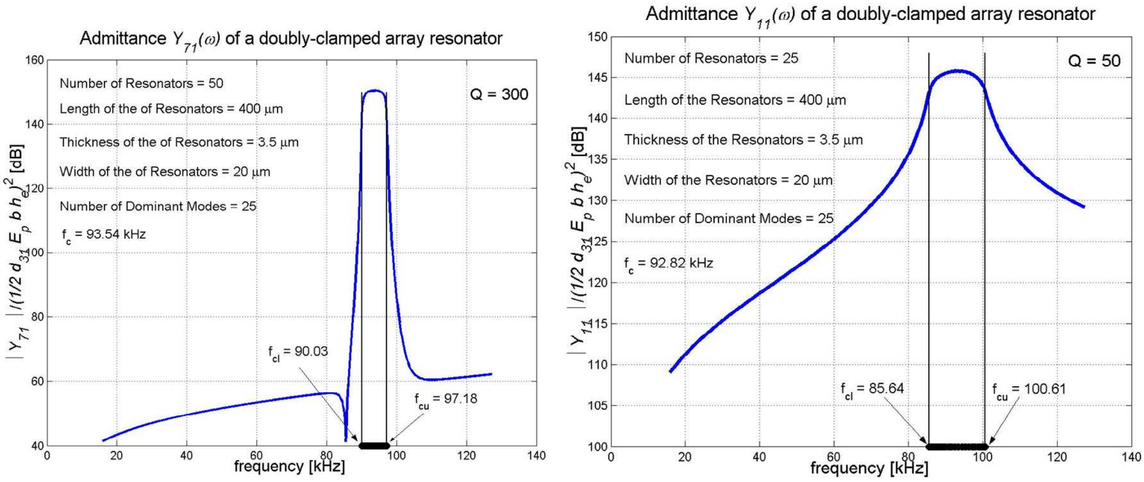

Figure 17: Representative amplitude response of two doubly-clamped AlGaAs composite beam resonator arrays.

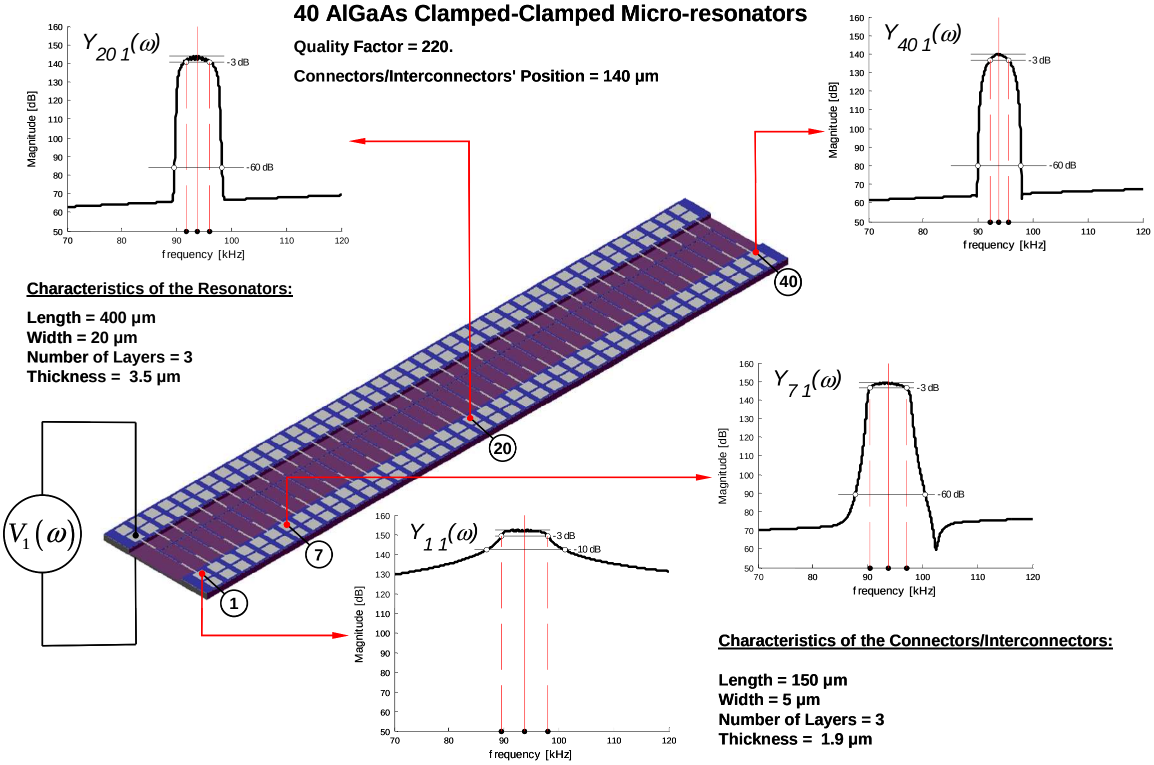

Figure 18: Representative admittance functions of a 40 doubly-clamped AlGaAs composite beam resonator array.

4 CONCLUSIONS

In this work, a semi-analytical computational mechanics model of a composite microstructure with piezoelectric actuation and piezoelectric sensing has been developed as a design tool for microresonators and microresonator arrays. The developed dynamic model of microresonators accounts for structural properties and the electromechanical coupling effect through finite element analysis. The dynamic admittance model is derived by combining the linear piezoelectric constitutive equations with the modal transfer function of the multilayered microresonator structure. The resonator receptance matrix is constructed through modal summation by considering only a limited number of dominant modes. The electromechanical coupling determination at the input and output ports makes use of the converse and direct piezoelectric effects. The developed model has been validated by comparing it with results available in the literature for clamped-clamped resonators. The numerical results are found to be in good agreement with the experimental measurements. The numerical simulations show that the consideration of axial loads is important to predict the natural frequencies of the resonators studied in the experiments. The microresonators studied in this work, which are used as micromechanical filters, are important for mobile communication systems and signal processing applications. It is believed that the numerical and analytical efforts presented in this work can be used as a basis to develop design tools for such systems.

REFERENCES

Balachandran, B. and Preidikman, S.. Oscillations of Piezoelectric Microscale Resonators. Progress in Computational Structures Technology, Chapter 13, pp. 327–352, Saxe-Coburg Publications, Stirling, Scotland, 2004.

Balachandran, B. Oscillations of Micro-Scale Resonators. Proceedings of the Fourth

International Conference on Smart Materials, Structures, and Systems, Bangalore, India, Paper No. SE01, July, 2005.

Ballato, A. Modeling piezoelectric and piezomagnetic devices and structures via equivalent networks. *IEEE Transactions on Ultrasonics, Ferroelectrics, and Frequency Control*, 48(5):1189–1240, 2001.

Chen, B. Cheeseman, B. A., Safari, A, Danforth, S. C. and Chou, T-W. Theoretical and Numerical Predictions of the Electromechanical Behavior of Spiral-Shaped Lead Zirconate Titanate (PZT) Actuators. *IEEE Transactions on Ultrasonics, Ferroelectrics, and Frequency Control*, 49(3):319–326, 2002.

Currano, L. Experimental and Finite Element Analysis of Piezoelectrically Driven MEMS Actuators. M.S. Thesis, Department of Mechanical Engineering, University of Maryland, College Park, 2002.

DeVoe, D. L. Piezoelectric Thin Film Micromechanical Beam Resonators. *Sensors and Actuators A (Physical)*, 88:263–272, 2001.

Lin, L., Howe, R., and Pisano, A. P. Microelectromechanical filters for signal processing. *Journal of Microelectromechanical Systems*, 7(3):286–294, 1998.

Nguyen, C. Microelectromechanical filters for miniaturized low-power communications. Proceedings of the SPIE Symposium on Smart Structures and Materials (Smart Electronics and MEMS), Newport Beach, CA, March, 1–5, 1999.

Pierkarski, B., DeVoe, D., Dubey, M., Kaul, R., and Conrad, J. Surface micromachined piezoelectric resonant beam filters. *Sensors and Actuators A (Physical)*, 91:313-320, 2001.

Preidikman, S., Li, H., and Balachandran, B. Forced Oscillations of Microelectromechanical Resonators. Proceedings of the ASME International Mechanical Engineering Congress and Exposition, Washington, D. C., Paper No. IMECE2003-44552, 2003.

Preidikman, S. and Balachandran, B. A Semi-analytical Tool Based on Geometric Nonlinearities for Microresonator Design. *Journal of Micromechanics and Microengineering*, 16:512–525, 2006.

von Preissig, F. J. and Kim, E. S. Topics in Finite-Element Modeling of Piezoelectric MEMS. International Conference on Modeling and Simulation of Microsystems, MSN, 2000.

Wang, J. S. and Ostergaard, D. F. A Finite Element-Electric Circuit Coupled Simulation Method for Piezoelectric Transducer. 1999 IEEE ULTRASONICS SYMPOSIUM, 1999.

Wang, K., Yu, Y., Wong, A.-C., and. Nguyen, C. T.-C. VHF free-free beam high-Q micromechanical resonators. *Journal of microelectromechanical systems*, 9(3):347–360, 2000.